ABSTRACT

Title of thesis: AB INITIO DETERMINATION OF KINETICS FOR ATOMIC LAYER DEPOSITION MODELING

Elizabeth M. Remmers, Master of Science, 2014

Thesis directed by: Professor Raymond A. Adomaitis
Department of Chemical and Biomolecular Engineering

A first principles model is developed to describe the kinetics of atomic layer deposition (ALD) systems. This model requires no fitting parameters, as it is based on the reaction pathways, structures, and energetics obtained from quantum-chemical studies. Using transition state theory and partition functions from statistical mechanics, equilibrium constants and reaction rates can be calculated. Several tools were created in Python to aid in the calculation of these quantities, and this procedure was applied to two systems- zinc oxide deposition from diethyl zinc (DEZ) and water, and alumina deposition from trimethyl aluminum (TMA) and water. A Gauss-Jordan factorization is used to decompose the system dynamics, and the resulting systems of equations are solved numerically to obtain the temporal concentration profiles of these two deposition systems.

AB INITIO DETERMINATION OF KINETICS FOR ATOMIC LAYER DEPOSITION MODELING

by

Elizabeth M. Remmers

Thesis submitted to the Faculty of the Graduate School of the
University of Maryland, College Park in partial fulfillment
of the requirements for the degree of
Master of Science
2014

Advisory Committee:

Professor Raymond A. Adomaitis, Chair
Professor Panagiotis Dimitrakopoulos
Professor Sheryl E. Ehrman

Acknowledgments

I owe my gratitude to all the people who have made this thesis possible and who made my graduate experience one that I will cherish forever.

First and foremost I'd like to thank my advisor, Ray Adomaitis. I couldn't have asked for a kinder, more understanding guide through this (terrifying at times!) process. I'd also like to thank everyone I worked with at WIE, especially Paige and Bria. I grew more than you know just learning by your examples, and I will always treasure the memories and advice I have from you both.

I also couldn't have done this without the support of my wonderful family. To my darling mother, for always knowing when to ask what's wrong and when to say nothing at all. To my dad, for showing me how to stay calm in the face of a storm. And to my brother Mike, for teaching me that the things I learned and the ways I've grown throughout these years runs so much deeper and means so much more than a degree.

I wouldn't have been able to maintain my sanity without the help of my bruh squad- Daniela, Kim, Alex and Ashley. Sometimes I just needed some kitten therapy, sometimes I needed to eat massive amounts of bacon, or to ponder the nature of the universe, and sometimes I just needed to dance. Thank you for always being down for any and everything! To my bestie Rodney, thank you for always being there when I needed to vent the rage, anxiety, existential crises... and for never failing to cheer me up. And to my darling Zachi, thank you for reminding me not to take it all so seriously.

Table of Contents

List of Tables

List of Figures

1
Introduction

1.1 Atomic Layer Deposition Overview

Atomic layer deposition (ALD) is a thin film deposition process used to create highly conformal films with precise control of thickness and composition. ALD utilizes a cycle of sequential, self-limiting surface reactions to deposit the desired film one monolayer or sub-monolayer during each cycle. Typically, a binary sequence of gaseous precursors is used, with purge periods in between to prevent gas phase reactions. The self-limiting nature of the deposition half-reactions arises from surface saturation due to a finite density of surface reaction sites, or steric hindrance when precursor ligands remain after the chemisorption reactions.

ALD was developed in the 1970s for manufacture of electroluminescent flat panel displays and experienced a resurgence in interest in the 1990s for use in microelectronics processing [Leskelä and Ritala(2003)]. The advantages of ALD over other thin film deposition techniques are precise thickness control, good conformality over high aspect ratio structures, and low process temperature. These

advantages make ALD a desirable process for microelectronics applications including high-k gate oxide deposition for MOSFETs, DRAM trench capacitor dielectrics, 3D multi-gate field effect transistors, and nonvolatile memory devices [Leskelä and Ritala(2003), Kim *et al.*(2009)]. Photovoltaic applications include surface passivation layers on crystalline-Si cells [Werner *et al.*(2011)], as well as buffer and barrier layers in CIGS cells [Pimenoff(2012), Holmqvist(2013)]. ALD also finds use in numerous other applications such as nanostructured self-cleaning surfaces [Ng *et al.*(2008)], protective coatings for spacecraft surfaces [Cooper *et al.*(2008)] and glass displays [Pimenoff(2012)], as well as solid lubricant oxides used in various devices including MEMS [Kim *et al.*(2009)] and automotive components [Doll *et al.*(2009)].

1.2 Overview of ALD Modeling Work

ALD modeling work falls into two main categories: empirical methods which require fitting parameters based on experiments (such as [Holmqvist *et al.*(2012), Holmqvist *et al.*(2013)]), and first principles (or *ab initio*) methods which do not. First principles methods allow for the exploration of novel processes, and can provide information about reaction pathways, substrate effects, and precursor decomposition [Elliott(2012)]. First principles ALD studies frequently utilize density functional theory (DFT) calculations to determine reaction pathways and energetics that in turn can be incorporated in reaction rate expressions, such as those derived from transition state theory (TST), to determine reaction kinetics. This kinetics information is used to compare the effect of different surface functional groups on reaction

rates [Xu and Musgrave(2004), Xu and Ye(2010)], or to explain experimentally observed differences in growth rate due to different precursor pulsing sequences in the deposition of HfO_2/Al_2O_3 mixtures [Nyns *et al.*(2010)]. Kinetics information can further be fed into a reactor model or kinetic Monte Carlo (kMC) simulation to determine the mechanism behind experimentally observed behavior such as the temperature dependency of growth rate [Deminsky *et al.*(2004)], or to predict desirable operating conditions [Travis and Adomaitis(2013b)].

1.3 Thesis Objectives

Despite these extensive efforts into understanding the fundamental aspects of ALD surface reaction mechanisms and integration of surface reaction models with reactor-scale precursor transport models (see [Holmqvist(2013)] for an excellent review), a fundamental understanding of how one models the surface species dynamics during the different phases of an ALD processing cycle and how these models connect to the more extensively studied chemical vapor deposition (CVD) processes is lacking.

The objective of this thesis is to develop a rational framework to compute reaction dynamics from first principles and transition state theory. Then, to simplify solution of these complex systems, the growth dynamics will be decomposed into three distinct types: the relatively slow deposition reactions, the fast equilibrium reactions, and the instantaneous processes which are governed by conservation principles.

In this thesis, this modeling framework will be applied to two deposition systems of interest, zinc oxide (ZnO) and alumina (Al_2O_3). The kinetics will be developed, the dynamics decomposed, and the resulting equations solved for the time evolution of the reaction systems.

2
Zinc Oxide System

2.1 Zinc Oxide Deposition Reaction Scheme

First, we will consider the relatively straightforward zinc oxide ALD reaction to develop the modeling framework, then apply the same procedure to the more complex alumina ALD reaction system. The overall ALD reaction to deposit solid zinc oxide using diethyl zinc and water as precursors can be written as the following:

$$ZnEt_2(g) + H_2O(g) \rightarrow ZnO(s) + 2EtH(g)$$

However, in the actual ALD process this reaction is a bit more complex. The precursors are introduced to the reactor in separate pulses, with purge periods of an inert gas in between to prevent the precursors from mixing and causing undesired gas phase reactions. The overall reaction can be split into two surface half-reactions, each utilizing one of the gaseous precursors.

Both half-reactions proceed with the same basic mechanism- barrierless adsorption takes place between the gas molecule and a surface site, forming an adsorbed adduct. This adduct can then form a transition state leading to a 1-2

hydrogen transfer reaction which liberates a molecule of ethane. Each half-cycle generates the precursor surface sites needed for the following half-cycle. And after two half-cycles, solid ZnO is incorporated into the bulk film.

2.1.1 ZnO Metal Half-Reaction

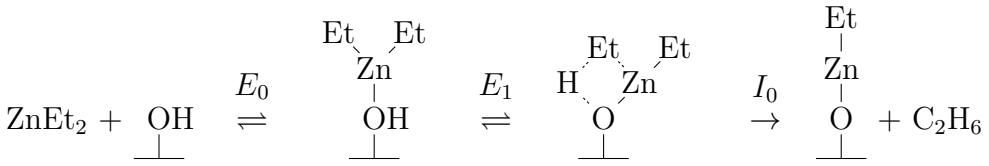

$Et_2Zn' + HO'$	Et_2ZnHO	$Et_2ZnHO^{\ddagger}$	$EtZn' + EtH$

The prime notation (O′ and Zn′) refers to coordinatively unsaturated species. In this case, the prime notation indicates 2-coordinate zinc and oxygen species.

The equilibrium constants and rates of these reactions may be formulated in the following way for the metal incorporation half reaction:

$$K_0 = \frac{[Et_2ZnHO]}{[Et_2Zn'][HO']} \quad \mathrm{m}^3 \tag{2.1}$$

$$K_1 = \frac{[Et_2ZnHO^{\ddagger}]}{[Et_2ZnHO]} \tag{2.2}$$

These equilibrium coefficient equations may be rearranged to find the following expressions which, when taken as a system of equations, can be solved for the concentrations of each species:

$$g_0: \quad 0 = K_0 \left(\frac{P_A}{k_B T} \right) [HO'] - [Et_2ZnHO] \qquad P_A > 0 \qquad (2.3)$$

$$g_0^o: \quad 0 = [Et_2ZnHO] \qquad P_A = 0 \qquad (2.4)$$

$$g_1: \quad 0 = K_1[Et_2ZnHO] - [Et_2ZnHO^{\ddagger}] \qquad P_A > 0 \qquad (2.5)$$

$$g_1^o: \quad 0 = [Et_2ZnHO^{\ddagger}] \qquad P_A = 0 \qquad (2.6)$$

Equations 2.4 and 2.6 are used during the purge and water pulse periods, when there is no diethyl zinc present in the reactor. Any ethane produced will be pumped out in the system exhaust, so we assume that reaction I_0 is irreversible and can express the reaction rate as the following:

$$f_0 = \frac{k_B T}{h} [Et_2ZnHO^{\ddagger}] \quad \mathrm{m^{-2}s^{-1}} \qquad (2.7)$$

2.1.2 ZnO Oxygen Half-Reaction

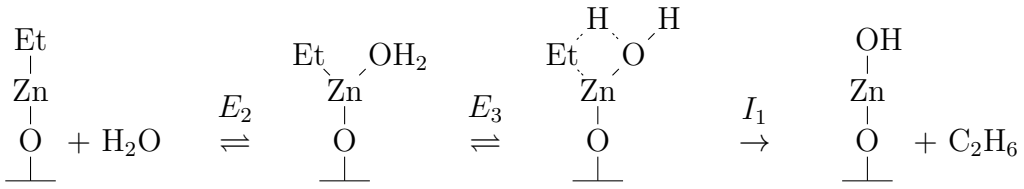

$EtZn' + H_2O'$	$EtZnH_2O$	$EtZnH_2O^{\ddagger}$	$HO' + ZnO + EtH$

The equilibrium coefficients and reaction rates of the oxygen incorporation half reaction are formulated as follows:

$$K_2 = \frac{[EtZnH_2O]}{[H_2O'][EtZn']} \quad \mathrm{m}^3 \tag{2.8}$$

$$K_3 = \frac{[EtZnH_2O^{\ddagger}]}{[EtZnH_2O]} \tag{2.9}$$

Again, these expressions may be rearranged to find:

$$g_2: \quad 0 = K_2 \left(\frac{P_B}{k_B T} \right) [EtZn'] - [EtZnH_2O] \qquad P_B > 0 \tag{2.10}$$

$$g_2^o: \quad 0 = [EtZnH_2O] \qquad P_B = 0 \tag{2.11}$$

$$g_3: \quad 0 = K_3[EtZnH_2O] - [EtZnH_2O^{\ddagger}] \qquad P_B > 0 \tag{2.12}$$

$$g_3^o: \quad 0 = [EtZnH_2O^{\ddagger}] \qquad P_B = 0 \tag{2.13}$$

As above, equations 2.11 and 2.13 are used during the purge and diethyl zinc pulse periods. The irreversible reaction rate may be expressed as the following:

$$f_1 = \frac{k_B T}{h} [EtZnH_2O^{\ddagger}] \quad \mathrm{m}^{-2}\mathrm{s}^{-1} \tag{2.14}$$

3
Ab Initio Calculations

Because of the near impossibility of experimentally measuring the dynamic ALD surface state in real time [Ott, *et al.*(1996)], researchers have turned to quantum chemical computations [Elliott(2012)] to evaluate reaction mechanisms and bond configurations and energetics. Taking the cited work a step further, we use statistical mechanics methods to compute the partition functions $\mathcal{Z}_i$ necessary to determine the equilibrium constants K_i based on the translational, vibrational, rotational, and electronic contributions to $\mathcal{Z}_i$.

3.1 Partition Functions

For reaction i involving species j with stoichiometric coefficients ν_j and the change in energy of the forward reaction $\Delta E_{0,rxn}$, we can write the equilibrium constant as:

$$K_i = e^{-\Delta E_{0,i}/k_B T} \prod \mathcal{Z}_j^{\nu_j} \tag{3.1}$$

Under the assumption that the translational, rotational, vibrational and elec-

tronic states are decoupled, the partition functions $\mathcal{Z}_i$ are separable as:

$$\mathcal{Z} = z_{trans} z_{rot} z_{vib} z_{el}$$

So, after defining the reactions that will comprise the reaction system, the next step is to calculate these partition functions for all species involved in the system.

3.1.1 Translational Component

The translational partition function of a polyatomic gas molecule is given by the following equation, derived from the particle in a box formulation:

$$z_{trans} = \left(\frac{2\pi m k_B T}{h^2} \right)^{3/2}$$

where m is the mass of the molecule, and k_B and h are the Boltzmann and Planck constants, respectively. The translational partition function is in units of m^{-3}, while all other partition function components that follow are unitless. Thus, the overall partition functions for the gas phase species have units of m^{-3} while the adsorbed species, which have no translational degrees of freedom have dimensionless partition functions.

3.1.2 Rotational Component

For a polyatomic gas molecule with symmetry factor σ and moments of inertia I_x, I_y, I_z the rotational partition function is as follows:

$$z_{rot} = \frac{\sqrt{\pi}}{\sigma} \sqrt{\left(\frac{8\pi k_B T}{h^2} \right)^3 I_x I_y I_z}$$

where the symmetry number σ is the number of equivalent configurations that can be obtained by rotating the molecule in three dimensions.

To calculate the partition function for internal rotations of molecules, these hindered rotations can be approximated as either harmonic oscillators or free rotors (or some combination of the two). At low frequencies, these rotations are accurately described by a free rotor whereas the harmonic oscillator approximation overestimates the partition function, approaching infinity as the frequency goes to zero. At higher frequencies, the harmonic oscillator approximation is more accurate whereas the free rotor approximation overestimates the partition function [Ayala and Schlegel(1998)]. We will use the free rotor formulation to approximate these modes, assuming that the relatively low process temperatures of ALD will keep rotational frequencies a bit lower, making this the more useful approximation.

Using the free rotor approximation, the partition function for internal rotational modes depends upon the moment of inertia I_i and symmetry factor σ_i of each mode as the following:

$$z_{rot} = \frac{\sqrt{\pi}}{\prod \sigma_i} \sqrt{\prod \left(\frac{8\pi^2 k_B T}{h^2} I_i \right)}$$

3.1.3 Vibrational Component

The vibrational partition function is the product of the contributions from each vibrational mode with frequency ν_i as the following:

$$z_{vib} = \prod_i \frac{e^{-h\nu_i/2k_BT}}{1 - e^{-h\nu_i/k_BT}}$$

which is derived by assuming that the vibrational modes are harmonic oscillators.

3.1.4 Electronic Component

The ground state electronic contributions are accounted for in the $e^{-\Delta E_0/k_B T}$ term of the equilibrium constant, so we do not account for this portion of the partition function separately. We also assume that the low process temperatures will keep the species in their ground state, so no additional electronic components are included.

3.2 Moment of Inertia Calculations

In order to calculate the partition functions, first we must calculate the moments of inertia of the gas molecules and the internal groups that we will be approximating as free rotors.

3.2.1 Gas Molecules as Rigid Bodies

Because gas molecules are able to freely rotate in space, they will tend to spin about axes which minimize the rotational energy; the same principle upon which gyroscopes operate. The moments of inertia along these principal axes are called the principal moments of inertia. To calculate the three principal moments of inertia for gas molecules, a python function was created which takes as input a matrix with

each row containing the mass and coordinates of each point mass in the molecule.

$$\begin{bmatrix} m_1 & x_1 & y_1 & z_1 \\ m_2 & x_2 & y_2 & z_2 \\ m_3 & x_3 & y_3 & z_3 \\ \dots & & & \end{bmatrix}$$

Any desired coordinate system may be used to define the locations of the masses, thus is often defined along symmetries for convenience. The point masses generally refer to atoms, but can equally be used to refer to moieties. The molecule is assumed to be a rigid body for this calculation, so that it may be easily described by fixed positions of the atoms (or moieties). The geometric configuration (bond angles and lengths) of these molecules can be found in relevant density functional theory (DFT) studies.

The function first determines if the origin used is the center of mass by checking if the sum of first moments along each direction is zero.

$$S_x = \sum m_i x_i = 0$$

$$S_y = \sum m_i y_i = 0$$

$$S_z = \sum m_i z_i = 0$$

The moment of inertia along any direction is at a minimum when it is about the axis which intersects the center of mass. These minimum moments of inertia are the desired values, so if these S_i values are nonzero, the program shifts the

coordinates to originate from the center of mass as:

$$x_{new} = x_{old} - \frac{S_x}{\sum m_i}$$

$$y_{new} = y_{old} - \frac{S_y}{\sum m_i}$$

$$z_{new} = z_{old} - \frac{S_z}{\sum m_i}$$

It then calculates the moment of inertia tensor I using the masses m_i and updated positions (x_i, y_i, z_i) of each point mass as the following:

$$I = \begin{bmatrix} I_{xx} & I_{xy} & I_{xz} \\ I_{xy} & I_{yy} & I_{yz} \\ I_{xz} & I_{yz} & I_{zz} \end{bmatrix}$$

$$= \begin{bmatrix} \sum m_i(y_i^2 + z_i^2) & \sum -m_i x_i y_i & \sum -m_i x_i z_i \\ \sum -m_i x_i y_i & \sum m_i(x_i^2 + z_i^2) & \sum -m_i y_i z_i \\ \sum -m_i x_i z_i & \sum -m_i y_i z_i & \sum m_i(x_i^2 + y_i^2) \end{bmatrix}$$

The diagonal elements I_{xx}, I_{yy} and I_{zz} contain the moments of inertia. The off diagonal elements $I_{ij}, i \neq j$ are the products of inertia, a measure of imbalance in mass distribution. If the products of inertia are all zero, this indicates that the coordinate system used is one of the principal axes of the system, thus the moments are the principal moments of inertia, the desired values. If the products of inertia are nonzero, the principal moments and axes are the eigenvalues and eigenvectors of the moment tensor, respectively [Thornton and Marion(2004)].

So the function then checks if the matrix is diagonalized, if so, the diagonal

elements are returned. If it is not diagonalized, the function goes on to calculate the eigenvalues of I, and returns those values as:

$$[I_x, I_y, I_z]$$

3.2.2 Internal and Adsorbed Moieties as Unhindered Rotors

Calculating the moments of inertia for adsorbed species and internal moieties represented by unhindered rotors proceeds a bit more simply as:

$$I = \sum m_i r_i^2$$

where r_i are the distances between the point masses m_i and the axis of rotation, which lies along the bond that connects the moiety to the molecule or the adsorbed species to the surface. Again, these geometric configurations may be determined from DFT studies, or for less complex rotating groups may be approximated by the expected standard geometry, such as the tetrahedral configuration for a rotating methyl group.

3.3 Vibrational Frequency Calculations

A helper function was also created to calculate the vibrational frequency of some bond between an adsorbate and surface. The function is called as the following:

$$vibFreq(MW_a, MW_s, \rho, r_o, E_o)$$

It takes the molecular weights of the adsorbate MW_a and substrate MW_s in g/mol, the density ρ of the substrate in g/cm^3, bond length r_o in m, and bond energy E_o

in eV. The mass of the adsorbate m_a is calculated by:

$$m_a = \frac{MW_a}{1000 \cdot N_{Avo}} = \frac{(g/mol)}{(g/kg)(molecules/mol)} = (kg/molecule)$$

and δ, the monolayer thickness of the substrate, is calculated by:

$$\delta = \sqrt[3]{\frac{MW_s}{\rho \cdot N_{Avo} \cdot 100^3}} = \left(\frac{(g/mol)}{(g/cm^3)(molecules/mol)(cm^3/m^3)}\right)^{1/3} = (m)$$

The bond energy is converted to units of J and then the vibrational frequency is calculated as the following:

$$\nu_0 = \frac{1}{2\pi}\sqrt{\frac{2\pi|E_o|r_o}{m_a\delta^3}} = \left(\frac{J \cdot m}{kg \cdot m^3}\right)^{1/2} = (1/sec)$$

3.4 Instantiating Species Objects

In order to simplify calculation of the partition functions of each species and to allow for easy reuse of species that participate in multiple reactions, a Python species class was developed which can create objects to represent various subclasses such as polyatomic gases and adsorbed species. Each subclass includes methods (class-specific functions) which calculate the partition functions. To instantiate one of these species objects requires the input of several attributes. The details of these two subclasses follow.

3.4.1 Polyatomic Gas

Species in the polyatomic gas class are instantiated as the following:

$$species.polyatomGas(\text{"}name\text{"}, MW, [\nu_1, \nu_2, ...], \sigma, [I_x, I_y, I_z, ...])$$

Inputs for these species include a string identifying the name of the species, the molecular weight MW in g/mol, a list of vibrational frequencies $[\nu_1, \nu_2, ...]$ in sec^{-1}, the rotational symmetry factor σ (which actually contains the product of the symmetry factors for all included modes), and a list of the three main moments of inertia of the molecule plus any additional internal rotations $[I_x, I_y, I_z, ...]$ in kg*m^2.

The method which calculates the translational partition function first converts the MW to mass per molecule m using Avogadro's number:

$$m = \frac{MW}{1000 \cdot N_{Avo}} = \frac{(g/mol)}{(g/kg)(molecules/mol)} = (kg/molecule)$$

Then it calculates $z_{trans}(T)$ according to:

$$z_{trans} = \left(\frac{2\pi m k_B T}{h^2}\right)^{3/2}$$

The rotational partition function method converts the moments of inertia into temperature units as:

$$\Theta_{rot,i} = \frac{h^2}{8\pi^2 I_i k_B} = \frac{(J*s)^2}{(kg*m^2)\left(\frac{J}{K}\right)} = (K)$$

Then the rotational partition function is calculated using the symmetry factor and the moments of inertia in temperature units as:

$$z_{rot} = \frac{\sqrt{\pi}}{\sigma}\sqrt{\prod \frac{T}{\Theta_{rot,i}}}$$

The vibrational partition function method first converts the vibrational frequencies to temperature units K as the following:

$$\Theta_{vib,i} = \frac{\nu_i * h}{k_B} = \frac{(s^{-1})(J*s)}{(\frac{J}{K})} = (K)$$

These are then used to calculate the vibrational partition function as:

$$z_{vib} = \prod_i \frac{e^{-\Theta_{vib,i}/2T}}{1 - e^{-\Theta_{vib,i}/T}}$$

And the method $pftrv(T)$ associated with this species subclass calls the partition function methods for the translational, rotational, and vibrational modes, then returns the product of these three. Because the translational PF returns its value in units of m^{-1} per each degree of freedom, the overall partition function for gas molecules will be in units of m^{-3}.

3.4.2 Adsorbed Molecule

Species in the adsorbed molecule class are instantiated as the following:

$$species.admolec(\text{"}name\text{"}, [\nu_1, \nu_2, ...], [I_1, I_2, ...], \sigma, AdType = \text{"}chem\text{"})$$

The inputs for this species are quite similar to those for the polyatomic gas species. One additional input is the adsorption type flag, which indicates that the species is chemisorbed (versus physisorbed, where AdType="phys").

Because all adsorbed species in this study are chemically bound to the surface, or chemisorbed, they have zero degrees of translational freedom and the translational partition function is:

$$z_{trans} = 1$$

These species can be bound to the surface by one or more bonds, so they may or may not have a mode representing the entire adsorbate rotating above the surface. They also may or may not include any additional internal rotations. The

σ should be the product of the symmetry factors for all included rotations. The calculations for the rotational partition function proceed as above in the polyatomic gas class.

Before instantiating the species, the frequencies of each vibrational mode are calculated as described in section 3.3. Then the vibrational partition function is calculated in the exact same way as the polyatomic gas class. An empty list may be used as input when no vibrational modes are to be considered, which results in $z_{vib} = 1$.

3.5 Calculating Equilibrium Constants

Upon instantiating all the species that participate in a reaction, we can use their partition function methods and the reaction energetics to calculate the equilibrium constant. As noted before, because we are separating out the reaction energetics we do not include the electronic partition functions, only the translational, rotational, and vibrational components.

A Python function was created to calculate the equilibrium constants of reactions involving the species objects described in the previous section. It takes as input the temperature T, the reaction energy $\Delta E_{0,rxn}$ and a list of tuples describing the reaction stoichiometry. This list is of the form:

$$[(\nu_1, species_1), (\nu_2, species_2), ...]$$

The program then proceeds to calculate the product of the partition functions

raised to their stoichiometric coefficients:

$$\prod \mathcal{Z}_i^{\nu_i}$$

by initializing a value $Qs = 1$ and then iterating through each species, multiplying Qs by the appropriate factor:

$$Qs \ast= \ species.pftrv(T)^{\nu}$$

where $species.pftrv(T)$ calls the method that contains the translational, rotational and vibrational contributions to the partition function for some species at temperature T.

This ratio of partition functions is then multiplied by the exponential term:

$$K = Qs * e^{-\Delta E_{0,rxn}/k_B T}$$

and this product K is returned.

4
Zinc Oxide Calculations

4.1 ZnO Partition Function Calculations

In order to calculate the partition functions of each species involved in the zinc oxide deposition reactions, we must decide which energy storage modes to include. The most important modes to include are those which are lost or gained during reaction, as the modes which are conserved will ultimately cancel in the equilibrium constant calculations.

4.1.1 Et_2Zn'

Starting with Et_2Zn', we must include the translational mode (simply by inputting the molecular weight into the polyatomic gas species object), the three main rotational modes of the entire molecule (calculated with the moment of inertia function using the geometry and mass information), as well as the internal rotations of both ethyl groups about their bonds to the central zinc atom. We neglect any vibrational modes, assuming that these modes will be conserved upon adsorption.

4.1.2 HO′

Then we consider the HO′ adsorption site. There is no translational freedom, but there is a rotation of this species about the bond from the surface to the O atom. There is also one vibrational mode included for this species, along the bond between the surface and the O atom. Although there is also a vibration between the O and H, we neglect this vibrational mode since it is small (because the H atom has a small mass) and it is unchanged by the adsorption reaction.

4.1.3 Et_2ZnHO

Next, we consider the adsorbed species Et_2ZnHO. As this is an adsorbed species, there is no translational freedom. The rotational modes included are the rotation of the entire adsorbate about the bond from the surface to the O atom, the rotation of the Et_2Zn group about the newly formed O-Zn bond, and the rotations of the two ethyl groups. To calculate the moments of inertia of these various rotations, we used the geometric information from the DFT study of [Afshar and Cadien(2013)]. We also include the vibrational mode of the newly formed bond, and the surface-O bond. It is important to include the vibration of the surface-O bond in both this species and the HO′ species, because although it is not a bond which breaks or forms during reaction, it changes in character since the mass of the adsorbate changes drastically.

4.1.4 $Et_2ZnHO^{\ddagger}$

The next species to look at is the transition state $Et_2ZnHO^{\ddagger}$. Again, there are no translational degrees of freedom. The rotations considered are the rotation of the entire species about the bond from the surface to the O atom, the rotation of one ethyl group, and the rotation of one methyl group. As the new bond formed is between the hydrogen and the innermost carbon of the ethyl moiety, this leaves a methyl group free to rotate. Here we include one vibrational mode between the surface and the Et_2ZnHO adsorbate. We do not include a vibrational mode to account for the newly formed bond, as it is part of a strained 4-member ring, limiting its ability to vibrate.

The rest of the species are defined in a similar manner, and the values of these partition functions are found in table 4.1.

Species	z_{trans}	z_{rot}	z_{vib}	$\mathcal{Z}_i$
Et_2Zn'	2.462×10^{33} m^{-3}	5.912×10^{7}	1	1.456×10^{41} m^{-3}
HO'	1	6.936	3.924	27.22
Et_2ZnHO	1	2.793×10^{6}	119.8	3.348×10^{8}
$Et_2ZnHO^{\ddagger}$	1	6526	11.31	73780
$EtZn'$	1	2299	92.89	2.135×10^{5}
H_2O'	1.372×10^{32} m^{-3}	79.44	1	1.090×10^{34} m^{-3}
$EtZnH_2O$	1	7124	453.6	3.232×10^{6}
$EtZnH_2O^{\ddagger}$	1	482.4	109.3	52750

Table 4.1: Partition Function Values for ZnO Species at $T = 450$ K.

4.2 ZnO Equilibrium Constant Calculations

Utilizing equation 3.1 and the partition function values calculated in the previous section, we can now compute the equilibrium constants for the four equilibrium

reactions in the ZnO deposition sequence.

K_i	Definition	Value	E_i (eV)	Source for E_i
K_0	$\left(\frac{\mathcal{Z}_{Et_2ZnHO}}{\mathcal{Z}_{Et_2Zn'}\mathcal{Z}_{HO'}}\right) e^{-E_0/k_BT}$	1.995×10^{-25} m^3	-0.837	[Afshar and Cadien(2013)]
K_1	$\left(\frac{\mathcal{Z}_{Et_2ZnHO^\ddagger}}{\mathcal{Z}_{Et_2ZnHO}}\right) e^{-E_1/k_BT}$	1.735×10^{-19}	1.35	[Afshar and Cadien(2013)]
K_2	$\left(\frac{\mathcal{Z}_{EtZnH_2O}}{\mathcal{Z}_{H_2O'}\mathcal{Z}_{EtZn'}}\right) e^{-E_2/k_BT}$	1.072×10^{-24} m^3	-0.794	[Afshar and Cadien(2013)]
K_3	$\left(\frac{\mathcal{Z}_{EtZnH_2O^\ddagger}}{\mathcal{Z}_{EtZnH_2O}}\right) e^{-E_3/k_BT}$	2.450×10^{-20}	1.59	[Afshar and Cadien(2013)]

Table 4.2: Equilibrium constant values for DEZ reactions at $T = 450$ K.

4.3 ZnO Reaction Factorization

Following the reaction factorization procedure outlined in [Remmers *et al.*(under revision)] (see Appendix A for the relevant section of this paper), we can obtain the fast, slow, and instantaneous modes of a reaction system based on the material balances of each species.

The factorization procedure takes the following matrix equation, where **c** contains the concentrations of each species, **S** contains the stoichiometric coefficients of each species in the various reactions contained in **r**.

$$\frac{d}{dt}\mathbf{c} = \mathbf{Sr} \tag{4.1}$$

Then it finds some transformation **U** such that **US** is as close to the identity

matrix **I** as possible. This transformation is applied to equation 4.1, resulting in:

$$\frac{d}{dt}\mathbf{Uc} = \mathbf{USr} \tag{4.2}$$

$$\frac{d}{dt}\mathbf{y} = \begin{bmatrix} \mathbf{I} \\ \\ \mathbf{0} \end{bmatrix} \mathbf{r} \tag{4.3}$$

where **y** is the new coordinate system of species.

Note that the g_i equilibrium expressions as defined in section 2.1 appear in units of m^{-2}, while the expressions below clearly are in units of $\mathrm{m}^{-2}\mathrm{s}^{-1}$. In order to represent the rates of these expressions when they are not at equilibrium, they should be multiplied by the frequency factor $\frac{k_B T}{h}$ s^{-1}, but as we assume they are at equilibrium, the values of g_i are zero and this factor is unnecessary.

Fast Modes:

$$g_0 = \frac{d}{dt}(-[Et_2Zn']) \tag{4.4}$$

$$g_1 = \frac{d}{dt}(-[Et_2ZnHO] - [Et_2Zn']) \tag{4.5}$$

$$g_2 = \frac{d}{dt}(-[H_2O']) \tag{4.6}$$

$$g_3 = \frac{d}{dt}([EtZnH_2O^{\ddagger}] - [Et_2Zn'] + [HO']) \tag{4.7}$$

Slow Modes:

$$f_0 = \frac{d}{dt}(-[Et_2ZnHO] - [Et_2Zn'] - [Et_2ZnHO^{\ddagger}]) \tag{4.8}$$

$$f_1 = \frac{d}{dt}(-[Et_2Zn'] + [HO']) \tag{4.9}$$

Instantaneous Modes:

$$0 = \frac{d}{dt}(-[H_2O'] + [Et_2ZnHO] + [Et_2Zn'] + [Et_2ZnHO^{\ddagger}] + [EtZn']) \tag{4.10}$$

$$0 = \frac{d}{dt}([Et_2ZnHO] + 2[Et_2Zn'] + [Et_2ZnHO^{\ddagger}] - [HO'] + [EtH]) \tag{4.11}$$

$$0 = \frac{d}{dt}([EtZnH_2O^{\ddagger}] + [H_2O'] - [Et_2Zn'] + [HO'] + [EtZnH_2O]) \tag{4.12}$$

Then this system of differential-algebraic equations (DAE) may be solved for the time evolution of the species concentrations, based on some initial conditions and utilizing a numerical integration procedure.

4.4 ZnO Deposition Simulations

Now we solve the DAE system encompassing the material balances of the species in the zinc oxide ALD system to obtain the concentration profiles. Since the reactions as written in the DFT study of [Afshar and Cadien(2013)] are fairly simple, any bare zinc or oxygen sites would be unreactive, and would only serve to limit the number of available sites for deposition. Thus, we begin with a fully hydroxylated surface. The maximum concentration of hydroxyl groups is equal to the maximum concentration of Zn or O atoms on the surface, as there is a 1:1 ratio of Zn:O and only one hydroxyl group can adsorb per each zinc site. This value is the product of the number density of one unit cell of the ZnO surface and the monolayer

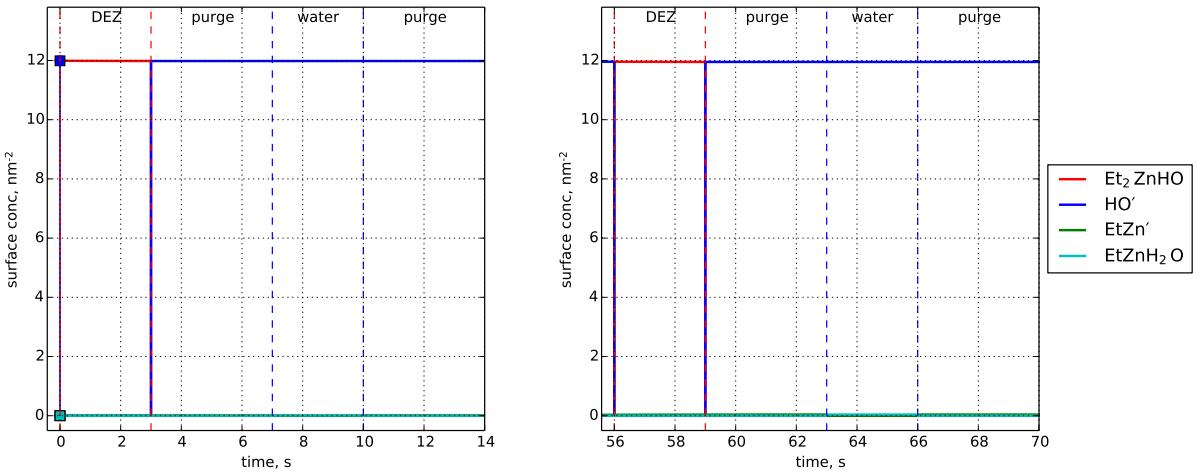

Figure 4.1: First cycle (left) and limit cycle (right) solutions corresponding to maximum hydroxylation ($\eta = 1$) at $T = 525$ K, showing no reactivity at normal experimental growth temperatures.

thickness.

$$\begin{aligned}[\hat{Zn}] = [\hat{O}] = [\hat{HO'}] &= \rho_N \cdot \Delta_Z \\ &= \rho_N^{2/3} \\ &= \left(\frac{\rho N_{Avo}}{MW_{ZnO}}\right)^{2/3} \\ &= 12\ nm^{-2}\end{aligned}$$

Using the maximum concentration of hydroxyl groups and zero concentrations for all other species as initial conditions, we numerically integrate the DAE to obtain the following concentration profiles. Unless otherwise indicated, precursor pulse times are 3 sec, purge times are 4 sec, and precursor partial pressures are at 2 Pa during the pulse periods for the following simulations.

As can be seen in figure 4.1, the forward reactions essentially cannot proceed at a process temperature of 525 K. We find a growth per cycle (gpc) of 0.0019 Å/cycle

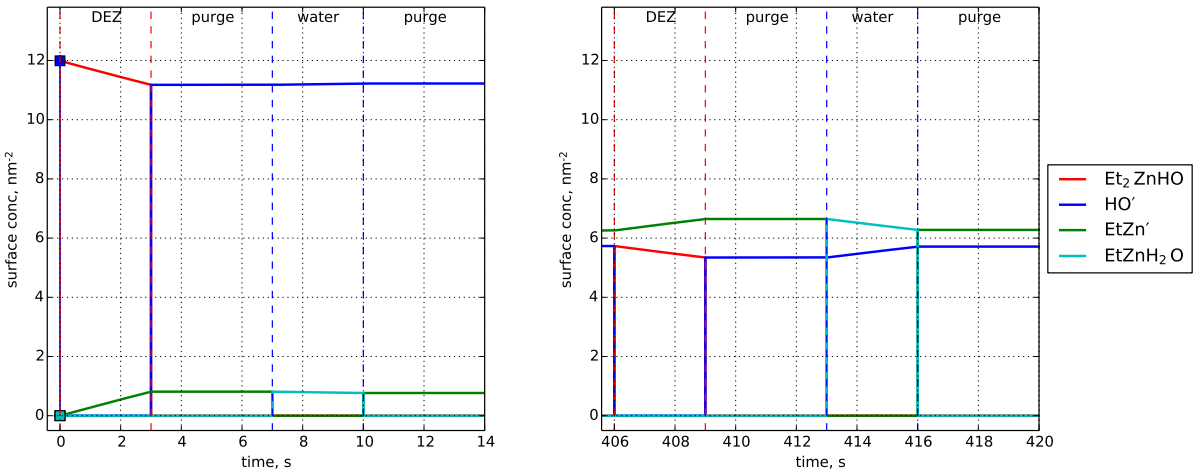

Figure 4.2: First cycle (left) and limit cycle (right) solutions corresponding to maximum hydroxylation ($\eta = 1$) at $T = 625$ K, showing limited reactivity at elevated growth temperatures.

according to this simulation. This conflicts with the experimental results of [Illiberi *et al.*(2012)] who obtained a gpc of 1.8 Å/cycle at this same temperature. During the DEZ pulse, we can see that the HO′ sites are all consumed as the equilibrium is reached between the surface and gas phase, but there appears to be insufficient thermal energy to drive the forward reaction to decompose Et_2ZnHO. Thus, when the purge period begins, all of the unreacted Et_2ZnHO species convert back to HO′ sites as the DEZ desorbs. As there are no EtZn′ sites for the water to adsorb on, no changes occur during the water pulse.

Even when we increase the temperature to 625 K, there is still very little reactivity as seen in figure 4.2. We can see a small drop in the Et_2ZnHO species and a corresponding increase in the EtZn′ species, which are able to act as adsorption sites during the water pulse, but the $EtZnH_2O$ concentration is still too small to cause a significant forward reaction. In this case we find a gpc of 0.20 Å/cycle in

the first cycle, which drops down to 0.094 Å/cycle when the limit cycle solution is reached after about 30 cycles.

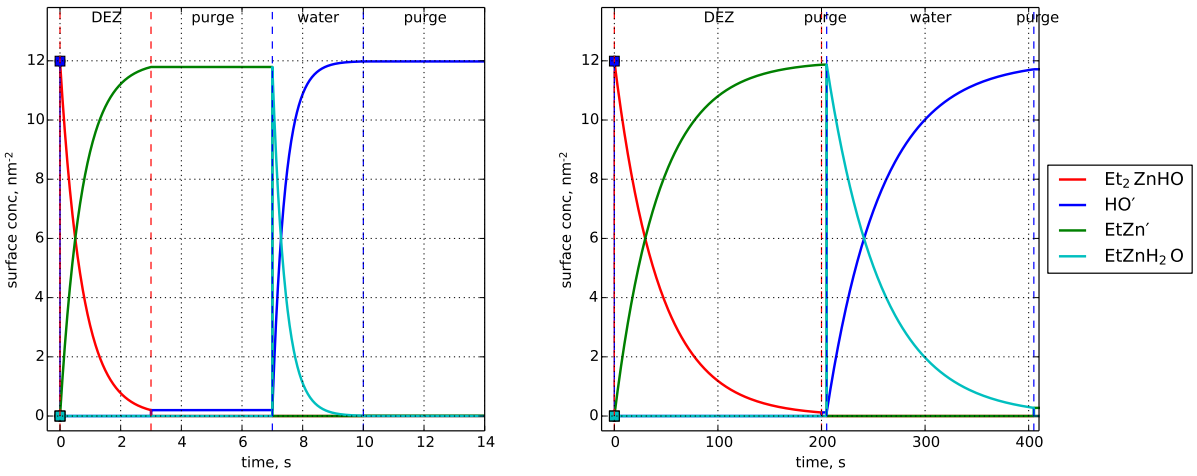

Figure 4.3: First cycle corresponding to a fully hydroxylated initial surface ($\eta = 1$) at elevated temperature of $T = 750$ K and normal dosing (left) and $T = 625$ K with increased precursor dose (right) showing the expected concentration profiles.

Only upon increasing the temperature to 750 K or the pulse times to 200 sec do we see the expected concentration profile for this deposition system, as seen in figure 4.3. The Et_2ZnHO concentration initially spikes up, then is depleted along with a corresponding increase in EtZn′. These act as adsorption sites for water, producing $EtZnH_2O$ which is then depleted as the HO′ sites are replenished. These cases both result in a gpc of 2.85 Å/cycle, which is approaching the monolayer thickness (2.9 Å), indicating near-saturating growth conditions. These simulations have no perceptible change in following cycles, indicating that they immediately reach the limit cycle solution and ALD growth conditions.

These simulation results indicate that something must be missing from this model. Increasing the precursor partial pressures had no effect on the simulation

results, demonstrating that the issue lies not in the adsorption step but somewhere in the subsequent activation and decomposition steps. Because increasing the process temperature or the precursor pulse times (to experimentally unrealistic levels) leads to a more reasonable concentration profile, we can speculate that the equilibrium coefficients for the K_1 and K_3 are too small, leading to too few activated, transition state species to drive the forward reactions. This could be because the reaction energetics are too high, or the entropy of the transition state is too low, due to some forgotten energetic modes.

The lack of alternative reaction pathways may also be contributing to these non-realistic results, as the intermediate species are all immediately lost at the start of the purge periods. If they were able to continue to react in the model, this might improve the yield.

The sharp changes in concentration at the switches from purge to pulse periods are also worrisome, and perhaps considering mass-transfer limited adsorption would make these transitions smoother.

5
Alumina ALD System

5.1 TMA and Water Reaction Scheme

After formulating the zinc oxide deposition system, we can move on to the more complex reaction system using TMA and water as precursors to deposit Al_2O_3. The overall reaction can be written as

$$2AlMe_3(g) + 3H_2O(g) \rightarrow Al_2O_3(s) + 6CH_4(g)$$

while the sequence of elementary steps is, of course, much more complicated.

5.1.1 TMA Reaction Sequence R0

The adsorption and subsequent reaction of gas-phase (monomer) TMA (Me_3Al') onto a surface with sufficient HO′ species can proceed through the following sequence of reactions to produce a surface populated with bare aluminum (Al′) sites. As noted before, the prime notation (O′ and Al′) is used to indicate coordinatively unsaturated species; for alumina films these are 2-coordinate O and 3-coordinate Al.

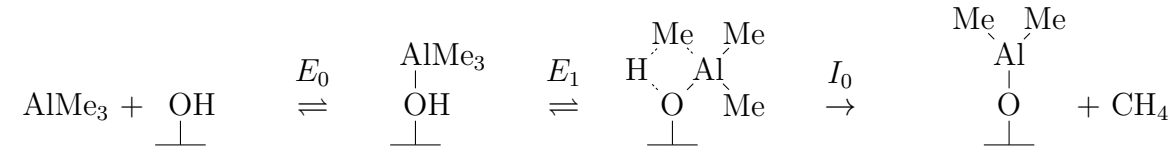

$Me_3Al' + HO' + 3S$	Me_3AlHO	$Me_3AlHO^{\ddagger}$	$Me_2Al' + Al' + MeH + S$

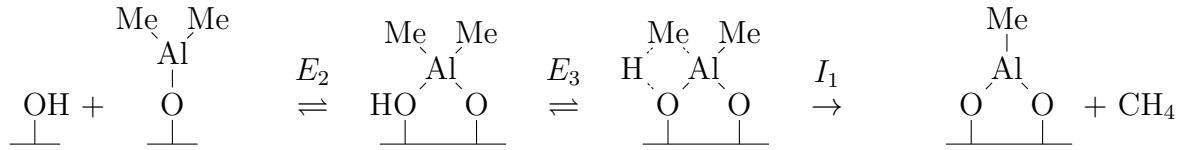

$HO' + Me_2Al'$	Me_2AlHO	$Me_2AlHO^{\ddagger}$	$MeAl' + Al' + MeH + S$

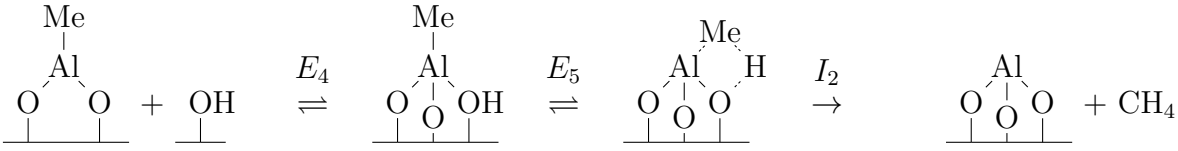

$MeAl' + HO'$	$MeAlHO$	$MeAlHO^{\ddagger}$	$Al' + MeH + S$

In the first equilibrium reaction E_0, gas phase TMA adsorbs onto a surface hydroxyl site HO' forming the surface adduct species we denote Me_3AlHO because of the 4-coordinate Al formed by this adsorption reaction. The oxygen likewise increases its coordinate number to three producing the HO group. We write the equilibrium relationship, noting that K_0 has units of volume, as

$$\mathrm{E}_0: \qquad K_0 = \frac{[Me_3AlHO]}{([S]/[\hat{S}])^3[Me_3Al'][HO']} \ \mathrm{m}^3 \tag{5.1}$$

where the effect of Me group steric hindrance is modeled by the $([S]/[\hat{S}])^3$ term. In all of the equilibrium and rate expressions to follow, we denote species surface concentration with $[\cdot]$ and maximum value by the hat $[\hat{}]$ notation. There must be three open surface sites S adjacent to the surface hydroxyl site for TMA to adsorb,

and the probability of finding an adjacent surface site is approximately $[S]/[\hat{S}]$. This equilibrium relationship (5.1) can be rearranged to find the algebraic equations

$$g_0: \quad 0 = K_0 \frac{P_A}{k_B T}[HO'] \frac{[S]^3}{[\hat{S}]^3} - [Me_3AlHO] \qquad P_A > 0 \qquad (5.2)$$

$$g_0^o: \quad 0 = [Me_3AlHO] \qquad P_A = 0 \qquad (5.3)$$

We note that two forms of g_0 are presented, depending on whether the TMA precursor is present; the explicit alternative function definition (denoted with the o superscript) for this and a subset of the subsequent reactions was found to improve computational stability in the simulation calculations.

The adsorbed adducts can undergo subsequent reactions. We compute the concentration of the activated complex $Me_3AlHO^{\ddagger}$ associated with the (1-2) H-transfer reaction in E_1 by

$$K_1 = \frac{[Me_3AlHO^{\ddagger}]}{[Me_3AlHO]}$$

giving

$$g_1: \quad 0 = K_1[Me_3AlHO] - [Me_3AlHO^{\ddagger}] \qquad P_A > 0 \qquad (5.4)$$

$$g_1^o: \quad 0 = [Me_3AlHO^{\ddagger}] \qquad P_A = 0 \qquad (5.5)$$

where (5.5) is used only in conjunction with (5.3). Finally, the rate of the irreversible reaction I_0 is simply

$$f_0 = \frac{k_B T}{h}[Me_3AlHO^{\ddagger}] \quad \mathrm{nm}^{-2}\mathrm{s}^{-1}$$

This reaction is considered irreversible because the gas-phase CH_4 produced by the reaction generally is pumped away from the growth surface in an ALD reactor.

The dimethyl species Me_2Al' produced by I_0 is considered unstable in the presence of neighboring surface HO′ species [Elliott and Greer(2004)]. The reaction between Me_2Al' and a neighboring surface HO′ to form an energetically favorable 4-coordinate Al is shown as reaction E_2; it is followed by a (1-2) H-transfer reaction involving equilibrium reaction E_3 and ejection of a methane molecule in reaction I_1. We can write the equilibrium relationship for E_2 as

$$K_2 = \frac{[Me_2AlHO]}{[Me_2Al'][HO']/[\hat{HO}]} \quad \text{so} \quad g_2 = [Me_2Al']\frac{[HO']}{[\hat{HO}]} - \frac{1}{K_2}[Me_2AlHO]. \quad (5.6)$$

Note that the equilibrium coefficient appears as $1/K_2$ in g_2 because $K_2 \gg 1$ (see Table 5.2). The activated complex surface concentration $[Me_2AlHO^{\ddagger}]$ then is computed from

$$K_3 = \frac{[Me_2AlHO^{\ddagger}]}{[Me_2AlHO]} \quad \text{and so} \quad g_3 = K_3[Me_2AlHO] - [Me_2AlHO^{\ddagger}] \quad (5.7)$$

which is used to compute the rate of reaction I_1 from

$$f_1 = \frac{k_B T}{h}[Me_2AlHO^{\ddagger}]. \quad (5.8)$$

We note the term $[HO']/[\hat{HO}]$ in (5.6) is used to approximate the probability of a HO′ group being located adjacent to the Me_2Al'. We also note that there are no alternative definitions to (5.6) and (5.7) for $P_A = 0$ because they are separated from

the adsorption reactions by irreversible reaction I_0 and so can continue during the purge periods.

The E_2, E_3, I_1 reaction subsequence produces species MeAlHO that initiates reaction subsequence E_4 E_5, I_2. Defining

$$K_4 = \frac{[MeAlHO]}{[MeAl'](\hat{[HO']}/\hat{[HO]})} \quad \text{thus} \quad g_4 = [MeAl']\frac{\hat{[HO']}}{\hat{[HO]}} - \frac{1}{K_4}[MeAlHO] \tag{5.9}$$

again noting the use of $1/K_4$ because $K_4 \gg 1$; we compute the activated complex surface concentration $[MeAlHO^{\ddagger}]$ from

$$K_5 = \frac{[MeAlHO^{\ddagger}]}{[MeAlHO]} \quad \text{so} \quad g_5 = K_5[MeAlHO] - [MeAlHO^{\ddagger}] \qquad \text{nm}^{-2} \tag{5.10}$$

to find the rate of I_2

$$f_2 = \frac{k_B T}{h}[MeAlHO^{\ddagger}] \qquad \text{nm}^{-2}\text{s}^{-1}. \tag{5.11}$$

Finally we observe that 3 Al′ surface species are created over this reaction sequence, with generation of the three Al′ evenly distributed between the three irreversible reaction steps. This must be the case because the overall reaction sequence effectively "uncovers" two Al species to which the HO′ were bonded, and one new Al′ is generated by the reaction sequence.

5.1.2 TMA Reaction Sequence R1

The Al′ sites created in reaction sequence R0 can react with water to produce a hydroxylated surface in the following way.

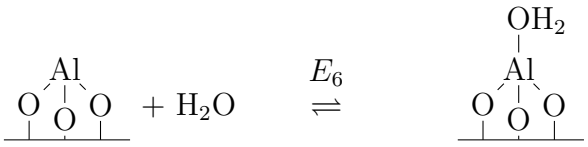

$Al' + H_2O'$	AlH_2O

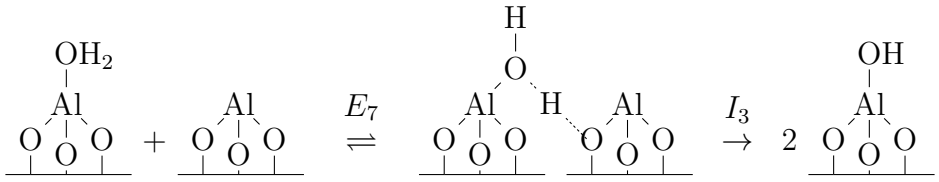

$AlH_2O + Al'$	$Al_2H_2O^{\ddagger}$	$2HO'$

This water sequence begins with the adsorption of H_2O' onto an Al' site in a Lewis acid-Lewis base adduct formation reaction in a manner essentially identical to E_0. The AlH_2O adduct forms an activated complex by reacting with a neighboring O', which we postulate must form one bond of a surface Al'. The irreversible reaction I_3 produces two surface hydroxyl groups. The products of I_3 are $(1+x)HO'+(1-x)HO+(1-x)Al'$. It may be useful to more carefully investigate HO versus HO' reactions; but for now, we take $x = 1$ and find the following rate and equilibrium expressions

$$g_6: \quad 0 = K_6 \frac{P_B}{k_B T}[Al'] - [AlH_2O] \qquad P_B > 0 \qquad (5.12)$$

$$g_6^o: \quad 0 = [AlH_2O] \qquad P_B = 0 \qquad (5.13)$$

$$g_7: \quad 0 = K_7[AlH_2O]\frac{[Al']}{[\hat{A}l]} - [Al_2H_2O^{\ddagger}] \qquad P_B > 0 \qquad (5.14)$$

$$g_7^o: \quad 0 = [Al_2H_2O^{\ddagger}] \qquad P_B = 0 \qquad (5.15)$$

with K_6 having units of volume, and the rate of I_3:

$$f_3 = \frac{k_B T}{h}[Al_2H_2O^{\ddagger}] \qquad (5.16)$$

Note that no steric hindrance effects are considered for the water reactions.

5.1.3 TMA Reaction Sequence R2

If there are not sufficient HO′ species on the surface during the TMA pulse, the TMA molecules may also adsorb onto oxygen bridges and proceed through the following reaction sequence, producing a methylated surface.

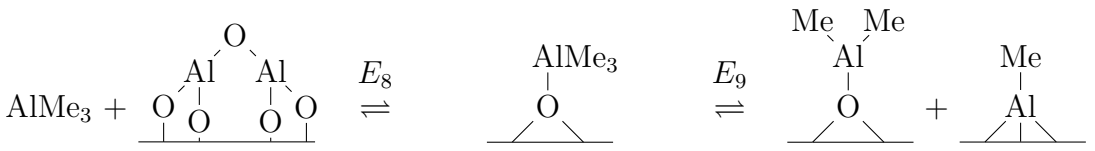

$Me_3Al' + 2Al' + 3S$	Me_3AlO	$Me_2Al'O + MeAl$

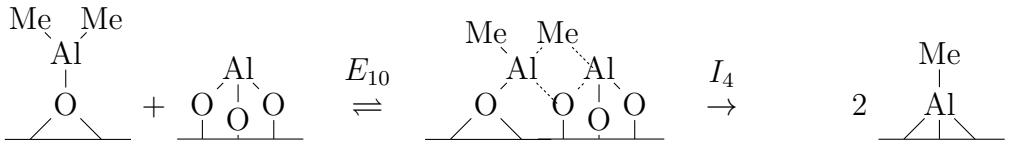

$Me_2Al'O + Al'$	$Me_2Al_2'^{\ddagger}$	2MeAl

The adsorption site of the first reaction of this sequence is a surface O′ bridge adjacent to two 3-coordinate surface Al′; the resulting equilibrium relationship is written in terms of $[Al']$ because just as in the water reaction discussed earlier, while the TMA reacts with the lone pair of electrons of the surface O′ the O′ must be adjacent to a surface Al′ site:

$$g_8: \quad 0 = K_8 \frac{P_A}{k_B T}[Al'] \frac{[Al']}{[\hat{A}l]} \frac{[S]^3}{[\hat{S}]^3} - [Me_3AlO] \qquad P_A > 0 \tag{5.17}$$

$$g_8^o: \quad 0 = [Me_3AlO] \qquad P_A = 0 \tag{5.18}$$

As with K_0, the equilibrium constant K_8 has units of volume.

The product of reaction E_8 proceeds through a barrierless dissociation step E_9 to produce dimethyl ($Me_2Al'O$) and monomethyl (MeAl) surface species. We write the equilibrium relationship of this decomposition reaction as

$$g_9: \quad 0 = [Me_3AlO][\hat{A}l] - \frac{1}{K_9}[Me_2Al'O][MeAl] \qquad P_A > 0 \tag{5.19}$$

$$g_9^o: \quad 0 = [Me_2Al'O] \qquad P_A = 0 \tag{5.20}$$

On locally bare growth surfaces (those with low HO′ concentration), $Me_2Al'O$ may react dissociatively with an adjacent Al′ surface site to produce two monomethyl aluminum surface species by the E_{10}, I_4 reaction sequence. The activated complex $Me_2Al_2'^{\ddagger}$ surface concentration and the rate of the subsequent irreversible reaction are computed by

$$g_{10}: \quad 0 = K_{10}[Me_2Al'O]\frac{[Al']}{[\hat{A}l]} - [Me_2Al_2'^{\ddagger}] \qquad P_A > 0 \tag{5.21}$$

$$g_{10}^o: \quad 0 = [Me_2Al_2'^{\ddagger}] \qquad P_A = 0 \tag{5.22}$$

and

$$f_4 = \frac{k_B T}{h}[Me_2Al_2'^{\ddagger}]. \tag{5.23}$$

Again, the ratio $[Al']/[\hat{A}l]$ is used to represent the fraction of neighboring surface Al sites that are bare. We note that I_4 is considered irreversible due to the large activation energy of the corresponding reverse reaction.

5.1.4 TMA Reaction Sequence R3

The methylated surface produced in reaction sequence R2 can proceed through the following pathway during the water pulse.

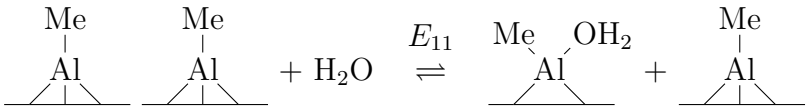

$2MeAl + H_2O'$	$MeAlH_2O + MeAl$

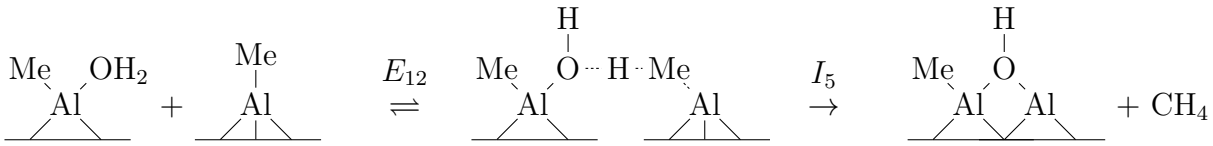

$MeAlH_2O + MeAl$	$Me_2Al_2H_2O^{\ddagger}$	$MeAlHO + Al' + S + MeH$

The reaction sequence begins with a water molecule adsorbing onto the Al atom in one of two adjacent MeAl surface species; we note that the Al of $MeAlH_2O$ retains its 4 coordination by breaking one of its O bonds. The adsorbed H_2O proceeds to react with the adjacent MeAl through a (1-4) H-transfer mechanism first by creating the critical complex $Me_2Al_2H_2O^{\ddagger}$, and then ejecting MeH in the irreversible I_5 reaction. In this final reaction step, we characterize the surface Al species created as Al′. The MeAlHO produced by I_5 ultimately results in the formation of MeH and Al′ by reactions E_5 and I_2.

For these reactions, we determine the following equilibrium expressions:

$$g_{11}: \quad 0 = K_{11}\frac{P_B}{k_B T}[MeAl]\frac{[MeAl]}{[\hat{A}l]} - [MeAlH_2O] \qquad P_B > 0 \qquad (5.24)$$

$$g_{11}^o: \quad 0 = [MeAlH_2O] \qquad P_B = 0 \qquad (5.25)$$

$$g_{12}: \quad 0 = K_{12}[MeAlH_2O]\frac{[MeAl]}{[\hat{A}l]} - [Me_2Al_2H_2O^{\ddagger}] \qquad P_B > 0 \qquad (5.26)$$

$$g_{12}^o: \quad 0 = [Me_2Al_2H_2O^{\ddagger}] \qquad P_B = 0 \qquad (5.27)$$

with K_{11} having units of volume, and the rate of I_5:

$$f_5 = \frac{k_B T}{h}[Me_2Al_2H_2O^{\ddagger}]. \qquad (5.28)$$

5.2 TMA Reaction Calculations

The partition functions for the alumina deposition species are calculated in the same way as the ZnO deposition species. The values for these partition functions are listed in table 5.1.

Using the calculated partition functions and the energetics obtained from DFT studies, the equilibrium constants for these reactions are calculated and values can be found in table 5.2.

Note that the equilibrium constants are calculated according to slightly different stoichiometry than the material balances, for example as seen in equilibrium reaction E_8. Because the partition function ratio is used to account for the changes in entropy during reaction, we are less concerned with the material balance bookkeeping aspects of the stoichiometry and more with the physical changes taking place.

Species	z_{trans}	z_{rot}	z_{vib}	$\mathcal{Z}_i$
Me_3Al'	1.098×10^{33} m^{-3}	468600	1	5.145×10^{38} m^{-3}
HO'	1	6.936	1	6.936
Me_3AlHO	1	34170	8.691	297000
$Me_3AlHO^{\ddagger}$	1	911.9	1	911.9
Me_2Al'	1	236.2	5.109	1207
Me_2AlHO	1	11.66	1	11.66
$Me_2AlHO^{\ddagger}$	1	4.547	1	4.547
$MeAl'$	1	4.547	1	4.547
$MeAlHO$	1	4.547	1	4.547
$MeAlHO^{\ddagger}$	1	1	1	1
H_2O'	1.372×10^{32} m^{-3}	79.44	1	1.090×10^{34} m^{-3}
Al'	1	1	1	1
AlH_2O	1	4.506	3.608	16.26
$Al_2H_2O^{\ddagger}$	1	1	1	1
O'	1	1	1	1
Me_3AlO	1	538.5	6.636	3573
$Me_2Al'O$	1	236.2	5.109	1207
$MeAl$	1	4.547	1	4.547
$Me_2Al_2^{\prime\ddagger}$	1	4.547	1	4.547
$MeAlH_2O$	1	11.56	4.202	48.57
$Me_2Al_2H_2O^{\ddagger}$	1	4.547	1	4.547

Table 5.1: Partition function values for TMA deposition species at $T = 450$ K.

The reaction factorization procedure results in $n_f = 13$ fast (algebraic equilibrium) modes, $n_s = 5$ slow ODEs in time, and $n_i = 4$ instantaneous (conserved quantities) modes for the $n_c = 22$ unique chemical species in this case. For this reaction system, some off-diagonal elements in **US** remain, since in this case $n_r = 19 > n_f + n_s$, indicating some interaction between the reactions and chemical species in this model.

Simulations for the alumina deposition system were computed from a starting point of 95% hydroxylation, which is reasonable given the fact that there is an alternate reaction pathway available for the bare alumina sites. So the initial conditions are 95% of the maximum possible HO' concentration, 5% of the max Al' concentra-

R_i	K_i	Definition	Value	E_i (eV)	Source for E_i
R_0	K_0	$\left(\frac{\mathcal{Z}_{Me_3AlHO}}{\mathcal{Z}_{Me_3Al'}\mathcal{Z}_{HO'}}\right)e^{-E_0/k_BT}$	5.753×10^{-27} m^3	-0.7	[Elliott and Greer(2004)]
R_0	K_1	$\left(\frac{\mathcal{Z}_{Me_3AlHO^\ddagger}}{\mathcal{Z}_{Me_3AlHO}}\right)e^{-E_1/k_BT}$	4.608×10^{-9}	0.52	[Widjaja and Musgrave(2002)]
R_0	K_2	$\left(\frac{\mathcal{Z}_{Me_2AlHO}}{\mathcal{Z}_{Me_2Al'}\mathcal{Z}_{HO'}}\right)e^{-E_2/k_BT}$	14.99	-0.36^*	[Elliott and Greer(2004)]
R_0	K_3	$\left(\frac{\mathcal{Z}_{Me_2AlHO^\ddagger}}{\mathcal{Z}_{Me_2AlHO}}\right)e^{-E_3/k_BT}$	2.418×10^{-13}	1.09^*	[Elliott and Greer(2004)]
R_0	K_4	$\left(\frac{\mathcal{Z}_{MeAlHO}}{\mathcal{Z}_{MeAl'}\mathcal{Z}_{HO'}}\right)e^{-E_4/k_BT}$	1.829×10^{12}	-1.17^*	[Elliott and Greer(2004)]
R_0	K_5	$\left(\frac{\mathcal{Z}_{MeAlHO^\ddagger}}{\mathcal{Z}_{MeAlHO}}\right)e^{-E_5/k_BT}$	6.179×10^{-15}	1.21	[Delabie *et al.*(2012)]
R_1	K_6	$\left(\frac{\mathcal{Z}_{AlH_2O}}{\mathcal{Z}_{H_2O'}\mathcal{Z}_{Al'}}\right)e^{-E_6/k_BT}$	3.056×10^{-22} m^3	-1.01	[Hass *et al.*(1998)]
R_1	K_7	$\left(\frac{\mathcal{Z}_{Al_2H_2O^\ddagger}}{\mathcal{Z}_{AlH_2O}\mathcal{Z}_{Al'}}\right)e^{-E_7/k_BT}$	0.005309	0.095	[Hass *et al.*(1998)]
R_2	K_8	$\left(\frac{\mathcal{Z}_{Me_3AlO}}{\mathcal{Z}_{Me_3Al'}\mathcal{Z}_{O'}}\right)e^{-E_8/k_BT}$	1.910×10^{-22} m^3	-1.2	[Elliott and Greer(2004)]
R_2	K_9	$\left(\frac{\mathcal{Z}_{Me_2Al'O}\mathcal{Z}_{MeAl}}{\mathcal{Z}_{Me_3AlO}}\right)e^{-E_9/k_BT}$	46350	-0.4	[Elliott and Greer(2004)]
R_2	K_{10}	$\left(\frac{\mathcal{Z}_{Me_2Al_2'^\ddagger}}{\mathcal{Z}_{Me_2Al'O}\mathcal{Z}_{Al'}}\right)e^{-E_{10}/k_BT}$	5.451×10^{-11}	0.7^*	[Elliott and Greer(2004)]
R_3	K_{11}	$\left(\frac{\mathcal{Z}_{MeAlH_2O}}{\mathcal{Z}_{H_2O'}\mathcal{Z}_{MeAl}}\right)e^{-E_{11}/k_BT}$	2.211×10^{-25} m^3	-0.74	[Delabie *et al.*(2012)]
R_3	K_{12}	$\left(\frac{\mathcal{Z}_{Me_2Al_2H_2O^\ddagger}}{\mathcal{Z}_{MeAlH_2O}\mathcal{Z}_{MeAl}}\right)e^{-E_{12}/k_BT}$	3.751×10^{-6}	0.33	[Delabie *et al.*(2012)]

Table 5.2: Equilibrium constant values for TMA reactions at $T = 450$ K. Values of E_i that are estimated from plots in their listed sources are marked with an (*).

tion and the maximum concentration of surface sites S (as there are no adsorbed ligands blocking these sites initially). We numerically integrate the DAE to obtain the following concentration profiles. Precursor pulse times are 1 sec, purge times are 5 sec, and precursor partial pressures are at 2 Pa during the pulse periods for the following simulations.

The alumina deposition simulations correlate much more closely with experimental data. As we can see in figure 5.1, the surface sites deplete to near zero

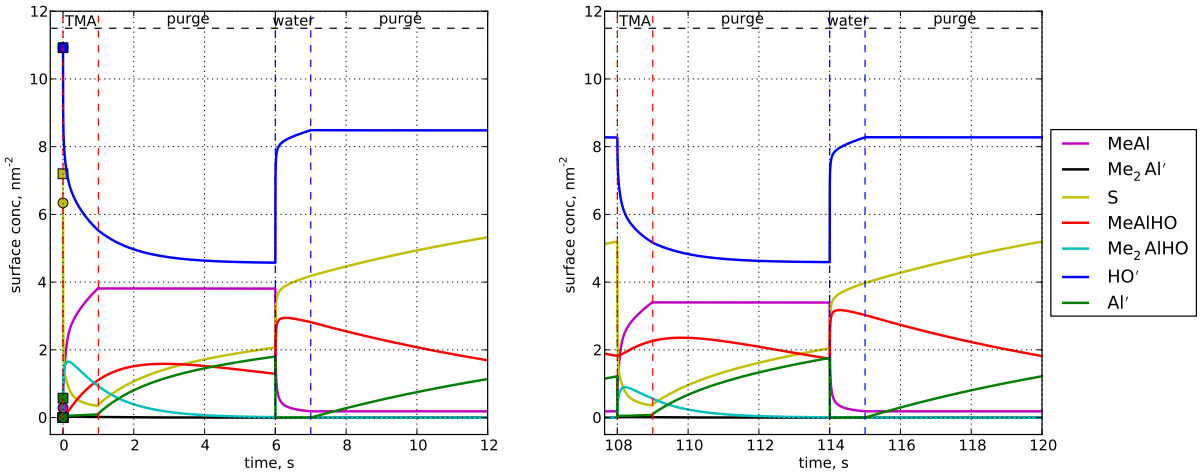

Figure 5.1: First cycle (left) and limit cycle (right) solutions corresponding to $\eta = 0.95$ at $T = 450$ K.

during the TMA pulse, indicating that the adsorption is limited by steric hindrance of the methyl ligands. We can also see that the TMA adsorbs quite rapidly on the bare alumina sites, indicated by the almost instantaneous drop of [Al′] to zero at the start of the precursor pulse.

Also of note is the fact that the concentration profiles continue to change throughout the purge periods. This is due to the surface reactions which are separated from the adsorption steps by irreversible reactions. These purely surface reactions continue to alter the surface state when the precursor gas is shut off, while the simpler zinc oxide deposition model does not have this capability.

These reaction conditions result in a gpc of 0.59 Å/cycle which is reasonable given that the system does not appear to reach saturation. Experimentally measured maximum growth rates for alumina ALD at $T = 450$ K are reported as 1.1 Å/cycle by [Ott, *et al.*(1997)] and 1.25 Å/cycle by [Groner *et al.(2004)*]. And indeed, when we increase the precursor pulse times to allow the system to reach equilibrium, we

obtain a gpc of 1.22 Å/cycle for this model.

6
Conclusions and Future Work

The work in this thesis was motivated by the need for a greater understanding of ALD reaction dynamics. Two different ALD chemistries were explored, the zinc oxide and alumina deposition systems. The elementary reactions and energetics were determined from DFT studies, then kinetics were formulated from first principles. A rational framework and several tools were developed to aid in the calculation of these kinetics. A Gauss-Jordan factorization was then utilized to transform the species into a new coordinate system, separating the time scales to allow for easier numerical integration. Then, these DAE systems were solved at various process conditions to compare the kinetics models to experimental results.

Issues arose with the solution of the zinc oxide system, perhaps stemming from the oversimplification of the reaction network, or from neglected energy storage modes or the larger energy barriers which must be overcome to form the transition states in this system.

Future work should explore:

- the effects of mass-transport limited adsorption on deposition kinetics

- the system's approach to equilibrium from non-equilibrium initial conditions
- the physical significance of the species coordinates determined by the factorization procedure.

A

A simple deposition reaction scheme

To begin, consider a simplified deposition reaction where we define a gas-phase monomer M and dimer D precursor species and the equilibrium relationship between the two. In the context of thin-film deposition processes, each precursor molecule M can be thought of as containing a single atom of the material (species A) to be deposited. An irreversible monomer reaction with surface site X produces the deposited film species A:

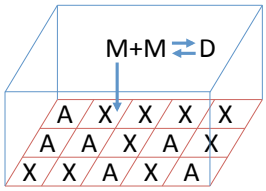

$$2\mathrm{M} \overset{g_0}{\rightleftharpoons} \mathrm{D} \qquad g_0 = \frac{1}{\epsilon}\left([M]^2 - \frac{1}{K_0}[D]\right) \text{ mol m}^{-3}s^{-1}$$

$$\mathrm{M} + \mathrm{X} \overset{f_0}{\rightarrow} \mathrm{A} \qquad f_0 = k_0[M][X] \qquad \text{mol m}^{-2}s^{-1}$$

where g_0 and f_0 are the net-forward equilibrium and deposition reaction rates, respectively. In our analysis, the rates associated with the equilibrium reactions are assumed to be much greater than that of deposition and so scaling the time appropriately, $g_0 = \mathcal{O}(1/\epsilon)$ with $\epsilon \ll 1$ and $f_0 = \mathcal{O}(1)$. By-products of the surface reactions are omitted in this simplified analysis. Writing the material balances for

each species give the four ODEs in time:

$$\frac{d\mathbf{c}^{n_c\times 1}}{dt} = \mathbf{S}^{n_c\times n_r}\mathbf{r}^{n_r\times 1} \quad \Longrightarrow \quad \frac{d}{dt}\begin{bmatrix} [M] \\ [D] \\ \sigma\,[X] \\ \sigma\,[A] \end{bmatrix} = \begin{bmatrix} -2 & -1 \\ 1 & 0 \\ 0 & -1 \\ 0 & 1 \end{bmatrix}\begin{bmatrix} g_0 \\ \sigma f_0 \end{bmatrix} \tag{A.1}$$

where σ = deposition surface area/reactant gas volume with units m^{-1}. The matrices $\mathbf{c}$, $\mathbf{S}$, and $\mathbf{r}$ contain the species concentrations, stoichiometric coefficients, and reaction rates respectively. n_c and n_r refer to the number of components and reactions.

Clearly, two issues arise at this point: (i) we have a higher-dimensional set of ODEs (four) relative to the single rate-limiting deposition step, and (ii) the monomer concentration dynamic behavior $[M](t)$ is governed by reaction rates of different orders of magnitude. Reducing (A.1) to its minimal dynamic dimension is straightforward using the QR factorization or the singular value decomposition. However, because array $\mathbf{S}$ represents reaction stoichiometry, not reaction rates, these decomposition methods will not provide guidance on separating time scales for the system. Therefore, the approach we pursue is based on the Gauss-Jordan factorization of $\mathbf{S}$ (see [Vora and Daoutidis(2001)] for a comparable approach). In (A.1), both dynamic dimension reduction and timescale separation can be accomplished if there exists a transformation $\mathbf{y} = \mathbf{U}\mathbf{c}$ in which the objective is to determine a new reactant coordinate system $\mathbf{y}$ such that *to the greatest extent possible, each reaction becomes*

associated with a single new reactant $y_i \in \mathcal{R}^{n_c}$, i.e.,

$$\mathbf{U}^{n_c \times n_c}\mathbf{S}^{n_c \times n_r} \approx \begin{bmatrix} \mathbf{I}^{n_r \times n_r} \\ \mathbf{0}^{(n_c - n_r)\times n_r} \end{bmatrix}.$$

We deliberately state this as an approximation to allow for off-diagonal elements of the matrix product **US** that appear in certain cases to be described later. The case $n_r > n_c$ will not be considered in this work. For our example system, we can factor the ODEs above by hand to find

$$\frac{d\mathbf{y}}{dt} = \frac{d}{dt}\begin{bmatrix} [D] \\ -[M] - 2[D] \\ \sigma[X] - [M] - 2[D] \\ \sigma[A] + [M] + 2[D] \end{bmatrix} = \frac{d}{dt}\begin{bmatrix} z_0 \\ x_0 \\ w_0 \\ w_1 \end{bmatrix} = \begin{bmatrix} 1 & 0 \\ 0 & 1 \\ 0 & 0 \\ 0 & 0 \end{bmatrix}\begin{bmatrix} g_0 \\ \sigma f_0 \end{bmatrix} \tag{A.2}$$

resulting in the following temporal modes for the specific case $k_0 = 1\ \mathrm{m^3 mol^{-1} s^{-1}}$, $K_0 = 1\ \mathrm{m^3 mol^{-1}}$, and $\sigma = 1\ \mathrm{m^{-1}}$:

$$\text{fast (equilibrium)} \quad \frac{dz_0}{dt} = \frac{d[D]}{dt} = \frac{1}{\epsilon}\left([M]^2 - [D]\right) \tag{A.3}$$

$$\text{slow (deposition)} \quad \frac{dx_0}{dt} = \frac{d(-[M] - 2[D])}{dt} = [M][X] \tag{A.4}$$

$$\text{instantaneous (species conservation)} \quad w_0 = [X] - [M] - 2[D] \tag{A.5}$$

$$w_1 = [A] + [M] + 2[D] \tag{A.6}$$

or, when the factorization (A.2) can be completed,

$$\text{slow} \qquad \frac{d\mathbf{x}}{dt} = \frac{d\mathbf{U}_x\mathbf{c}}{dt} = \mathbf{f}(\mathbf{c}) \qquad\qquad \frac{d\mathbf{x}}{dt} = \mathbf{f}(\mathbf{x},\mathbf{z},\mathbf{w}_o) \tag{A.7}$$

$$\text{fast} \qquad \frac{d\mathbf{z}}{dt} = \frac{d\mathbf{U}_z\mathbf{c}}{dt} = \frac{1}{\epsilon}\mathbf{g}(\mathbf{c}) \qquad \stackrel{\epsilon\to 0}{\Longrightarrow} \qquad 0 = \mathbf{g}(\mathbf{x},\mathbf{z},\mathbf{w}_o) \tag{A.8}$$

$$\text{instantaneous} \qquad \mathbf{w}_o = \mathbf{U}_w\mathbf{c} \tag{A.9}$$

where for $\epsilon \to 0$ we find the *semi-explicit* differential-algebraic (DAE) system where $\mathbf{x}$ are the differential variables, $\mathbf{z}$ the algebraic variables, and $\mathbf{y}^\intercal = [\mathbf{x}^\intercal\, \mathbf{z}^\intercal\, \mathbf{w}_o^\intercal]$ [Biegler(2000)]. We observe the "instantaneous" modes correspond to conserved quantities: constant w_1 is simply the total number of deposition element atoms in our control volume and $w_0 + w_1 = [X] + [A]$ arises from the conservation of surface states - that for every A created by the deposition reaction, one X is consumed.

Again, we note the strong resemblance of this decomposition approach to other nonlinear model reduction procedures (see e.g., [Baldea, Daoutidis and Kumar(2006),Kumar, Christofides, and Daoutidis(1998),Sujit, Torres, and Daoutidis(2011), Vora and Daoutidis(2001)]). Likewise, this species conservation is at work in systems such as the isomerization reactions of [Wei and Prater(1962)] and numerous follow-up studies (e.g., [Lombardo and Hall(1971)]) where the eigenvector associated with a single zero eigenvalue of the *reaction rate coefficient* array represents the conservation of species $A_1 + A_2 + A_3$ in the equilibrium reaction network shown below:

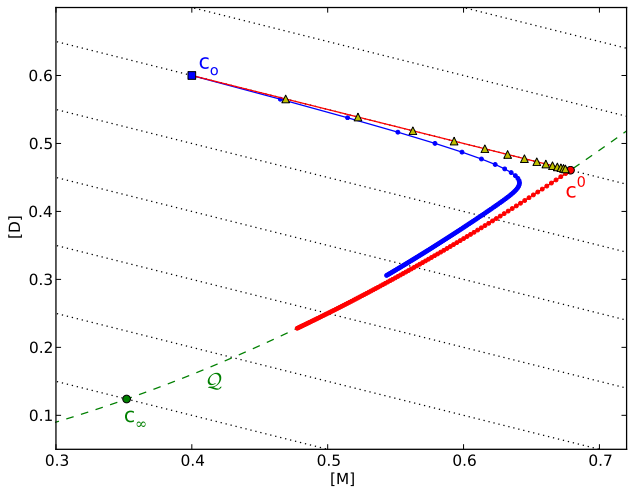

Figure A.1: *Two-dimensional dynamics with* $k_0 = K_0 = 1$, $\epsilon = 0.1$, $\sigma = 1$, *and* $t \in [0, 2]$. *Original initial conditions and those projected onto the equilibrium manifold (green dashed curve* $\mathcal{Q}$*) are marked with the filled blue square and red circle, respectively. Each point denotes 0.02 time units; black dotted lines denote* $[M] + 2[D] =$ *constant.*

$$
\begin{array}{ccc}
 & A_1 & \\
k_{21} \nearrow\!\!\swarrow k_{12} & & k_{13} \searrow\!\!\nwarrow k_{31} \\
 & k_{23} & \\
A_2 & \rightleftharpoons & A_3 \\
 & k_{32} &
\end{array}
$$

A.1 Time integration

Other than being stiff for $\epsilon \ll 1$, direct numerical integration of (A.4-A.6) subject to initial conditions $\mathbf{c}_o = \mathbf{c}(t = 0)$ is relatively straightforward: (1) the initial conditions are translated to the new chemical coordinate system $\mathbf{y}_o = \mathbf{U}\mathbf{c}_o$ to determine the initial values $\mathbf{x}_o$, $\mathbf{z}_o$, and $\mathbf{w}_o$, of the slow, fast, and instantaneous modes, respectively; (2) the ODEs then are integrated in time in terms of $\mathbf{x}$ and $\mathbf{z}$, computing the reaction rates using current values of the concentration determined from $\mathbf{c} = \mathbf{U}^{-1}\mathbf{y}$. We note that $\mathbf{U}$ must be invertible because the forward elimination

procedure used to compute it is reversible, and that $\mathbf{w} = \mathbf{w}_o$ for all time. Representative results for (A.4-A.6) obtained using a fixed step-size implicit Euler integrator are shown in Fig. A.1 for $\mathbf{c}_o = [0.4, 0.6, 1, 0]^\intercal$ resulting in $x_o = -1.6$, $z_o = 0.6$, and $\mathbf{w}_o = [-0.6, 1.6]^\intercal$ illustrating the rapid contraction from the initial condition $\mathbf{c}_o$ to the neighborhood of the equilibrium manifold $\mathcal{Q}$ and the subsequently slower dynamics which follow.

Multiplying (A.3) through by ϵ, we observe that our reaction system is a *singularly perturbed ODE* system for $\epsilon \ll 1$: setting $\epsilon = 0$ results in the loss of the fast dynamics in species space associated with relaxation to the manifold defined by the equilibrium conditions $\mathcal{Q} = \{\mathbf{c} : k_f[M]^2 - k_r[D] = 0\}$. Let us consider computing the outer solution only of the singular-perturbation problem [Nayfeh(1981)] subject to initial conditions $\mathbf{c}_o$ in the following manner:

(i) Project the initial conditions $\mathbf{c}_o$ onto the equilibrium manifold $\mathcal{Q}$ to find $\mathbf{c}^0$ by solving the set of nonlinear/linear algebraic equations:

$$\begin{bmatrix} \mathbf{U}_x\mathbf{c}^0 \\ \mathbf{g}(\mathbf{c}^0) \\ \mathbf{U}_w\mathbf{c}^0 \end{bmatrix} = \begin{bmatrix} \mathbf{x}_o \\ \mathbf{0} \\ \mathbf{w}_o \end{bmatrix}$$

(ii) Given the species state $\mathbf{c}^i$ at time t^i (where $i = 0$ for the projected initial state) compute:

$$\mathbf{x}^i = \mathbf{U}_x\mathbf{c}^i$$

(iii) Compute the implicit Euler update over time step Δ_t by driving the residual at right to zero using a Newton-Raphson or other technique suitable for nonlinear algebraic equations.

$$\begin{bmatrix} (\mathbf{x}^{i+1} - \mathbf{x}^i)/\Delta_t - \mathbf{f}\left(\mathbf{U}^{-1}\mathbf{y}^{i+1}\right) \\ \mathbf{g}\left(\mathbf{U}^{-1}\mathbf{y}^{i+1}\right) \\ \mathbf{w}^{i+1} - \mathbf{w}_o \end{bmatrix}$$

A demonstration of this method in the solution of (A.4-A.6) for $\epsilon = 0$ is shown in Fig. A.1 where one can see the initial specifications $\mathbf{c}_o$, the projection of these conditions into the equilibrium manifold $\mathcal{Q}$ to give the initial conditions $\mathbf{c}^0$, and time integration on the manifold approaching equilibrium point $\mathbf{c}_\infty$. Because our simple semi-explicit DAE is index-1 for all initial conditions $[M]_o \neq -1/4$, consistency of the initial conditions is not an issue for this example. However, more detailed deposition surface reaction models may have DAE index values that depend on initial states of the growth surface that are physically realizable (as opposed to the negative concentration for our demonstration system), necessitating more sophisticated treatment of the initial conditions [Biegler(2000), Pantelides(1988)].

A.2 Multiple (slow) deposition reactions

We can add the following reaction to describe a second mode of deposition directly from the dimer species

$$\text{D+X} \xrightarrow{f_1} \text{A+M} \qquad f_1 = k_1[D][X]$$

to find that the Gauss-Jordan factorization cannot be completed; however, the result still accomplishes the dimension reduction and time scale separation objectives. For $k_0 = k_1 = K_0 = 1$ we compute

$$\begin{aligned}
\text{slow} \quad & \frac{dx_0}{dt} = \frac{d([M] + 2[D])}{dt} = -[M][X] - [D][X] \\
\text{fast} \quad & \frac{dz_0}{dt} = \frac{d[D]}{dt} = \frac{1}{\epsilon}\left([M]^2 - [D]\right) - [D][X] \quad \overset{\epsilon \to 0}{\Longrightarrow} \quad [M]^2 - [D] = 0 \\
\text{instantaneous} \quad & w_0 = [X] + [A] \\
& w_1 = [A] + [M] + 2[D]
\end{aligned}$$

which are precisely the same conserved quantities (one reaction site X consumed for each surface A produced, and conservation of the deposited element found in species A, M, and D), the same equilibrium relationship, and a single dynamic mode describing the consumption of the total precursor supply by the combination of both surface reactions.

A.3 Non-physical solutions

To illustrate a potential numerical challenge introduced by the equilibrium relationships, consider

$$\mathrm{A} + \mathrm{B} \overset{g_0}{\rightleftharpoons} \mathrm{C} \quad \text{with} \quad \frac{d[A]}{dt} = -g_0, \quad \frac{d[B]}{dt} = f_0 - g_0, \quad \frac{d[C]}{dt} = g_0$$

where the concentration of species B is fed by a second reaction with constant rate f_0. Rewriting the material balances in matrix form

$$\frac{d}{dt}\begin{bmatrix} [C] \\ [B] \\ [A] \end{bmatrix} = \begin{bmatrix} 1 & 0 \\ -1 & 1 \\ -1 & 0 \end{bmatrix} \begin{bmatrix} g_0 \\ f_0 \end{bmatrix}$$

The factorization of this set of ODEs is trivial, resulting in

$[A] + [C] = w_0$ the instantaneous mode

$[B] + [C] = x_0 + \Delta_t f_0$ the slow mode evolving over time interval Δ_t

On the equilibrium manifold,

$$[C] - K_0[A][B] = 0$$

$$x_0 + \Delta_t f_0 - [B] - K_0 \left(w_0 - x_0 - \Delta_t f_0 + [B]\right)[B] = 0$$

Without loss of generality, we set $K_0 = 1$ and find

$$[B] = \frac{x_0 + \Delta_t f_0 - 1 - w_0 \pm \sqrt{(1 + w_0 - x_0 - \Delta_t f_0)^2 + 4(x_0 + \Delta_t f_0)}}{2}$$

From the initial state we can determine $x_0 = B(t = 0) + C(t = 0) \geq 0$ and so only the positive-root solution can be valid. While this result is unambiguous, it is nevertheless important because when $K_0 \gg 1$, the implicit numerical integration procedure can overshoot the limit of $[A] \to 0$ and converge upon the negative, and physically meaningless solution. Therefore, care must be taken in time-step size control in cases where the f_0 terms are significant and the equilibrium relationship favors the reaction product.

Bibliography

[Afshar and Cadien(2013)] Afshar, A. and K.C. Cadien, Growth mechanism of atomic layer deposition of zinc oxide: A density functional theory approach, *Applied Physics Letters* **103** 251906 (2013).

[Ayala and Schlegel(1998)] Ayala, P. Y. and H. B. Schlegel, Identification and treatment of internal rotation in normal mode vibrational analysis, *J. Chem. Phys.* **108** 2314 (1998).

[Baldea, Daoutidis and Kumar(2006)] Baldea, M., P. Daoutidis, and A. Kumar, Dynamics and control of integrated networks with purge streams, *AIChE J.* **52** 1460-1472 (2006).

[Biegler(2000)] Biegler, L. T., *Differential-Algebraic Equations (DAEs)*, Lecture notes (2000).

[Cooper *et al.*(2008)] Cooper, R., H. P. Upadhyaya, T. K. Minton, M. R. Berman, X. Du, and S. M. George, Protection of polymer from atomic-oxygen erosion using Al_2O_3 atomic layer deposition coatings, *Thin Solid Films* **516** 4036-4039 (2008).

[Delabie *et al.*(2012)] Delabie, A, Sioncke S, Rip J, Van Elshocht S, Pourtois G, Mueller M, Beckhoff B, Pierloot K (2012) Reaction mechanisms for atomic layer deposition of aluminum oxide on semiconductor substrates. J. Vac. Sci. Technol. A 30(1):01A127-1-01A127-10

[Deminsky *et al.*(2004)] Deminsky, M., A. Knizhnik, I. Belov, S. Umanskii, E. Rykova, A. Bagatur'yants, B. Potapkin, M. Stoker, and A. Korkin, Mechanism and kinetics of thin zirconium and hafnium oxide film growth in an ALD reactor, *Surface Science* **549** 67-86 (2004).

[Doll *et al.*(2009)] Doll, G. L., B. A. Manesh, H. Mohseni, and T. W. Scharf, Chemical vapor deposition and atomic layer deposition of coatings for mechanical applications, *J. Therm. Spray Techn.* **19** 510-516 (2009).

[Elliott(2012)] Elliott, S. D., Atomic-scale simulation of ALD chemistry, *Semicond. Sci. Technol.* **27** 074008 (2012).

[Elliott and Greer(2004)] Elliott, S. D. and J. C. Greer, Simulating the atomic layer deposition of alumina from first principles, *J. Mater. Chem.* **14** 3246-3250 (2004).

[Groner *et al.(2004)]* Groner, M. D., F. H. Fabreguette, J. W. Elam, and S. M. George, Low-temperature Al_2O_3 atomic layer deposition, *Chem. Mater.* **16** 639-645 (2004).

[Hass *et al.*(1998)] Hass, K. C., W. F. Schneider, A. Curioni, and W. Andreoni, The chemistry of water on alumina surfaces: reaction dynamics from first principles, *Science* **282** 265 (1998).

[Holmqvist(2013)] Holmqvist, A., *Model-based Analysis and design of Atomic Layer Deposition Processes*, PhD Thesis, Lund University (2013).

[Holmqvist *et al.*(2012)] Holmqvist, A., T. Törndahl, and S. Stenström, A model-based methodology for the analysis and design of atomic layer deposition processes–Part I: Mechanistic modelling of continuous flow reactors, *Chem. Eng. Sci.* **81** 260-272 (2012).

[Holmqvist *et al.*(2013)] Holmqvist, A., T. Törndahl, and S. Stenström, A model-based methodology for the analysis and design of atomic layer deposition processes–Part II: Experimental validation and mechanistic analysis, *Chem. Eng. Sci.* **94** 316-329 (2013).

[Illiberi *et al.*(2012)] Illiberi, A., F. Roozeboom and P. Poodt, Spatial atomic layer deposition of zinc oxide thin films, *ACS Applied Materials and Interfaces*, **4** 268-272 (2012).

[Kim *et al.*(2009)] Kim, H., H. Lee, and W. J. Maeng, Application of atomic layer deposition to nanofabrication and emerging nanodevices, *Thin Solid Films* **517** 2563-2580 (2009).

[Kumar, Christofides, and Daoutidis(1998)] Kumar, A., P. D. Christofides, P. Daoutidis, Singular perturbation modeling of nonlinear processes with non-explicit time-scale multiplicity, *Chem Engng Sci.* **53** 1491-1504 (1998).

[Leskelä and Ritala(2003)] Leskelä, M. and M. Ritala, Atomic layer deposition chemistry: recent developments and future challenges, *Angew. Chem. Int. Ed.* **42** 5548-5554 (2003).

[Lombardo and Hall(1971)] Lombardo, E. A. and W. K. Hall, Computerized catalytic kinetics: A useful extension of the method of Wei and Prater, *AIChE J.* **17** 1229-1233 (1971).

[Nayfeh(1981)] Nayfeh, A. H., *Introduction to Perturbation Techniques*, J. Wiley, New York, (1981).

[Ng *et al.*(2008)] Ng, C. J. W., H. Gao, and T. T. Y. Tan, Atomic layer deposition of TiO_2 nanostructures for self-cleaning applications, *Nanotechnology* **18** 445604 (2008).

[Nyns *et al.*(2010)] Nyns, L., A. Delabie, G. Pourtois, S. Van Elshochtm C. Vinckier, and S. De Gendt, Study of the surface reactions in ALD hafnium aluminates, *J. Electrochem. Soc.* **157** G7-G12 (2010).

[Ott, *et al.*(1996)] Ott, A. W., K. C. McCarthy, J. W. Klaus, J. D. Way, and S. M. George, Atomic layered controlled deposition of Al_2O_3 films using a binary reaction sequence chemistry, *Appl. Surf. Sci.* **107** 128-136 (1996).

[Ott, *et al.*(1997)] Ott, A. W., J. W. Klaus, J. M. Johnson, and S. M. George, Al_2O_3 thin film growth on Si(100) using binary reaction sequence chemistry, *Thin Solid Films* **292** 135-144 (1997).

[Pantelides(1988)] Pantelides, C. C., The consistent initialization of differential-algebraic systems, *SIAM J. Sci, Stat. Comput.* **9** 213-231 (1988).

[Pimenoff(2012)] Pimenoff, J., Atomic layer deposition: excellence in thin film coating, *Vak. Forsch. Prax.* /bf 24 6 (2012).

[Remmers *et al.*(under revision)] Remmers, E., C.D. Travis and R.A. Adomaitis, Reaction factorization for the dynamic analysis of atomic layer deposition kinetics, *Chemical Engineering Science*, (currently under revision).

[Sujit, Torres, and Daoutidis(2011)] Sujit, S. S., A. I. Torres, and P. Daoutidis, Networks with large solvent recycle: Dynamics, hierarchical control, and a biorefinery application, *AIChE J.* **58** 1764-1777 (2011).

[Thornton and Marion(2004)] Thornton, S. and J. B. Marion, *Classical Dynamics of Particles and Systems*, Fifth edition Brooks/Cole, (2004).

[Travis and Adomaitis(2013b)] Travis, C., D. and R. A. Adomaitis, Dynamic modeling for the design and cyclic operation of an atomic layer deposition (ALD) reactor, *Processes* **1** 128-152 (2013).

[Vora and Daoutidis(2001)] Vora, N. and P. Daoutidis, Nonlinear model reduction of chemical reaction systems, *AIChE J.* **47** 2320-2332 (2001).

[Wei and Prater(1962)] Wei, J. and C. D. Prater, The structure and analysis of complex reaction systems, *Adv. Catalysis* **13** 203-392 (1962).

[Werner *et al.*(2011)] Werner, F., W. Stals, R. Görtzen, B. Veith, R. Brendel, and J. Schmidt, High-rate atomic layer deposition of Al_2O_3 for the surface passivation of Si solar cells, *Energy Procedia* **8** 301-306 (2011).

[Widjaja and Musgrave(2002)] Widjaja, Y.; Musgrave, C.B. Quantum chemical study of the mechanism of aluminum oxide atomic layer deposition. *Appl. Phys. Lett* **2002**, *80*, 3304–3306.

[Xu and Ye(2010)] Xu, K. and P. D. Ye, Theoretical study of atomic layer deposition reaction mechanism and kinetics for aluminum oxide formation at graphene nanoribbon open edges, *J. Phys. Chem. C* **114** 10505-10511 (2010).

[Xu and Musgrave(2004)] Xu, Y. and C. B. Musgrave, A DFT study of the Al_2O_3 atomic layer deposition on SAMs: effect of SAM termination, *Chem. Mater.* **16** 646-653 (2004).

PUBLICATIONS & PRESENTATIONS

Accepted for Publication

Remmers, E., C.D. Travis and R.A. Adomaitis, Reaction factorization for the dynamic analysis of atomic layer deposition kinetics, *Chemical Engineering Science*, (currently under revision).

Conference Presentations

None